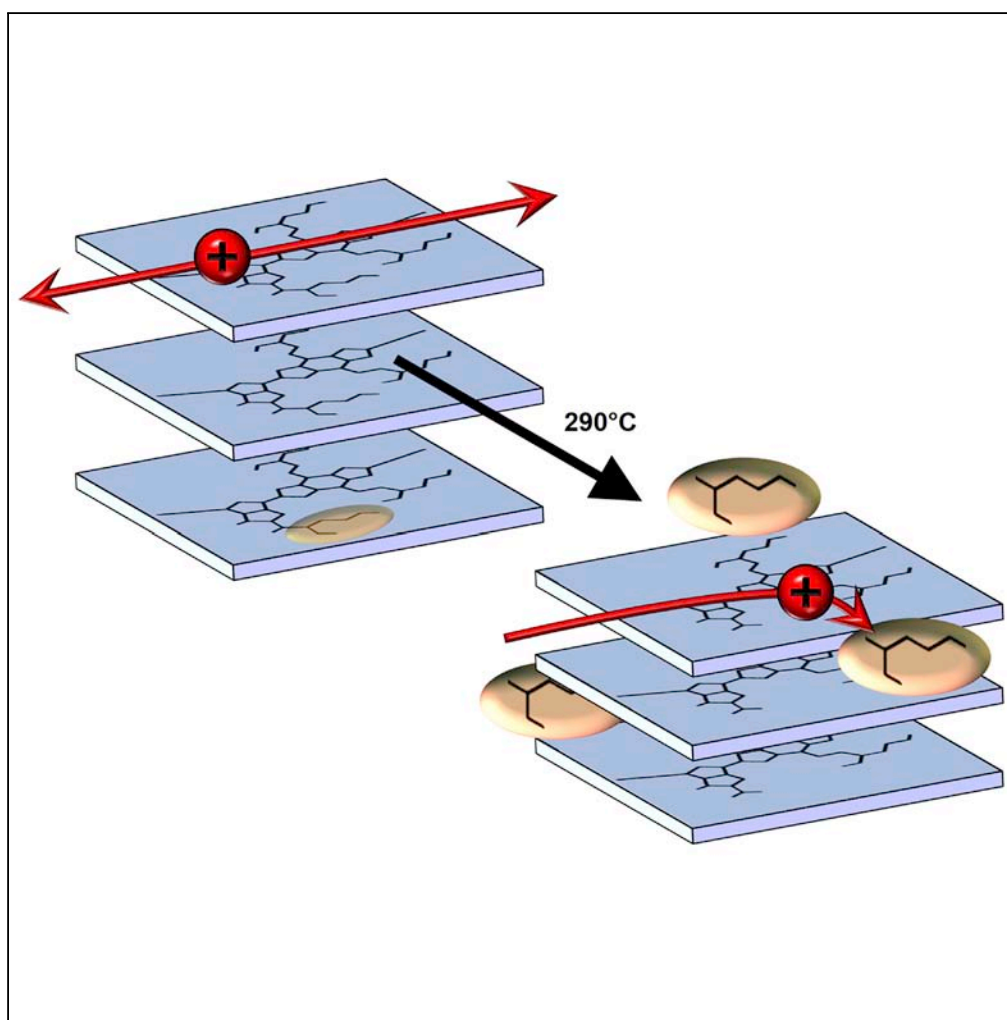


Article

Morphological, Chemical, and Electronic Changes of the Conjugated Polymer PTB7 with Thermal Annealing



Victoria Savikhin,
Lethy K.
Jagadamma,
Lafe J. Purvis, ...,
Christopher J.
Douglas, Ifor D.W.
Samuel, Michael F.
Toney

mftoney@slac.stanford.edu

HIGHLIGHTS

Annealing to 260°C improves morphology and hole mobility in PTB7-based thin films

Annealing to 290°C induces side-chain cleavage and closer packing of PTB7

Thermally cleaved PTB7 films resemble irradiated films, suggesting a burn-in mechanism

Release of trapped reaction by-products could result in improved device performance

Savikhin et al., iScience 2, 182–192
April 27, 2018 © 2018 The Author(s).
<https://doi.org/10.1016/j.isci.2018.03.002>

Article

Morphological, Chemical, and Electronic Changes of the Conjugated Polymer PTB7 with Thermal Annealing

Victoria Savikhin,^{1,2} Lethy K. Jagadamma,³ Lafe J. Purvis,⁴ Iain Robertson,³ Stefan D. Oosterhout,¹ Christopher J. Douglas,⁴ Ifor D.W. Samuel,³ and Michael F. Toney^{1,5,*}

SUMMARY

There is considerable interest in improving the performance of organic optoelectronic devices through processing techniques. Here, we study the effect of high-temperature annealing on the properties of the semiconducting polymer PTB7 and PTB7:fullerene blends, of interest as efficient organic photovoltaic (OPV) devices. Annealing to moderate temperature improves the PTB7 morphology and optoelectronic properties. High-temperature annealing also improves morphology but results in poorer optoelectronic properties. This is a result of side chain cleavage that creates by-products that act as trap states, increasing electronic disorder and decreasing mobility. We further observe changes to the PTB7 chemical structure after thermal cleavage that are similar to those following solar irradiation. This implies that side chain cleavage is an important mechanism in device photodegradation, which is a major “burn-in” loss mechanism in OPV. These results lend insight into side chain cleavage as a method of improving optoelectronic properties and suggest strategies for improvement in device photostability.

INTRODUCTION

Organic semiconducting films can be used for making efficient lighting (organic light-emitting diodes, or OLEDs), electronics with low production energy cost (organic field effect transistors, or OFETs [Kymissis, 2009]), and next-generation solar cells (organic photovoltaics, or OPVs). OPVs can be used to generate energy with near-zero CO₂ production and have many attractive features such as their potentially low cost, flexible form factor, and light weight. These desirable properties are especially important to bring solar energy to developing nations, where energy demand is growing fastest (BP, 2016) but the capital to invest in large-scale energy plants is not readily available.

Although these applications of organic semiconductors have different materials engineering goals, a fundamental understanding of the electronic and morphological properties of polymers and small organic molecules is crucial for the optimization of organic semiconductors. In particular, increasing charge carrier mobility is crucial for increasing the performance of organic electronic devices, and this requires an in-depth understanding of the relationship between microstructure and mobility. Polymers and small molecules for solution-processed devices typically consist of a semiconducting backbone and solubilizing, electrically insulating alkyl side chains (Vogelbaum and Sauvé, 2017). Charges are delocalized along the backbone, making intra-molecular charge transport effective, so average mobility can be limited by inter-molecular charge transport (hopping between chains). For polymers, it is often believed that inter-molecular hopping rate is inversely related to the distance between hopping sites and the amount of molecular disorder (Coropceanu et al., 2007). Thus, decreasing inter-molecular distance along the π - π stacking (hopping) direction is often considered a design rule for increasing mobility in conjugated polymers.

In this paper, we explore the effects of thermal annealing on the morphology and mobility of PTB7 (poly [[4,8-bis[(2-ethylhexyl)oxy]benzo[1,2-b:4,5-b']dithiophene-2,6-diyl][3-fluoro-2-[(2-ethylhexyl)carbonyl]thieno[3,4-b]thiophenediyl]]), a polymer with chemical structure shown in Figure 1A. The PTB7:PC₇₁BM ([6,6]-phenyl C₇₁ butyric acid methyl ester) bulk heterojunction (BHJ) is of interest because it is among the highest-performing OPV devices, achieving a power conversion efficiency of up to 9.15% (He et al., 2015). Thermal annealing to moderate temperatures has been shown to allow polymer chains to move into a more ordered configuration while fullerenes diffuse out of mixed regions, which can have a favorable effect on device properties

¹Stanford Synchrotron Radiation Lightsource, SLAC National Accelerator Laboratory, 2575 Sand Hill Road, Menlo Park, CA 94025, USA

²Electrical Engineering Department, Stanford University, 350 Serra Mall, Stanford, CA 94305, USA

³Organic Semiconductor Centre, SUPA, School of Physics and Astronomy, University of St. Andrews, St. Andrews, KY16 9SS, UK

⁴Department of Chemistry, University of Minnesota – Twin Cities, 207 Pleasant St SE, Minneapolis, MN 55455, USA

⁵Lead Contact

*Correspondence: mftoney@slac.stanford.edu
<https://doi.org/10.1016/j.isci.2018.03.002>



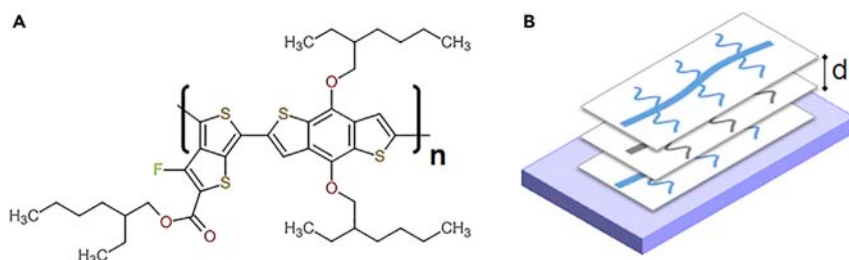


Figure 1. Polymer Structure

(A) Chemical structure of PTB7.

(B) Illustration of face-on packing of three PTB7 strands on a substrate. Thick lines represent polymer backbones and thin lines represent alkyl side chains. The π - π stacking distance is labeled "d."

(Verploegen et al., 2010). This process has been shown to be suppressed to some extent in PTB7:PC₇₁BM BHJs (Dkhil et al., 2017). Previous work has often focused on annealing of a BHJ blend, making it difficult to separate the effects of material nanophase segregation from the effects of polymer crystallization (Hedley et al., 2017). Thus we first focus on the properties of the neat film of PTB7 during and after thermal annealing, and then extend the results to the BHJ system.

Furthermore, high-temperature annealing steps have been shown to induce cleavage of alkyl side chains in many conjugated polymers. Although alkyl side chains are necessary to solubilize conjugated polymers, their insulating properties make them unfavorable for charge transport. Because of this, there has been considerable interest in eliminating these side chains through thermal cleavage (Sun et al., 2012). Thermo-cleavable side chains have been shown to have several advantages: increase in backbone planarity (Guo et al., 2015), increase in efficiency in some devices, improvement in device stability (Manceau et al., 2010; Helgesen et al., 2011), suppression of PCBM aggregation in blends (Vahdani et al., 2016), and decrease in solubility of the film, allowing multilayer processing (Kuhn et al., 2015). In many cases, cleavage occurs at the ester group, leaving a carboxyl group (Manceau et al., 2010; Helgesen et al., 2011) or removing the ester group entirely (Guo et al., 2015; Kuhn et al., 2015; Höfle et al., 2017; Hillebrandt et al., 2016). In polymers based on the poly(thieno[3,4-b]thiophene-benzo[1,2-b:4,5-b']dithiophene) (PTB) backbone, cleavage occurs at the ether group, yielding a hydroxyl group (Vahdani et al., 2016). Although the annealing temperatures used in this work are high, the literature has shown that the cleavage temperature can be reduced through inclusion of a catalyst, as in the case of Vahdani et al. (2016), or through engineering of side chains (Hillebrandt et al., 2016).

In this work, we show that moderate-temperature (260°C) annealing decreases the disorder in the PTB7 in neat and blend films with a corresponding increase in mobility in neat PTB7. Unexpectedly, annealing the polymer at temperatures above 260°C produces a previously unseen morphology with a smaller inter-molecular distance between PTB7 backbones in both neat and blend films. Our data suggest that this temperature results in a side chain cleavage reaction and this causes the smaller inter-molecular distance. In contrast to expectations, the mobility of this emerged polymorph is lower despite a decrease in morphological disorder, decrease in π - π stacking distance, and partial removal of insulating side chains. Furthermore, the decay of time-resolved photoluminescence becomes significantly faster after annealing to 290°C. We speculate that the presence of reaction by-products as trap states is responsible for these changes.

Previous work on photoinduced degradation of neat PTB7 yields similar FTIR and UV-Vis spectral changes to our 290°C annealed films (Son et al., 2011). Thus we suggest that formation of trap states is partially responsible for this burn-in performance loss in PTB7 and possibly in similar polymers as well (Upama et al., 2016; Mateker and McGehee, 2017). This indicates that side chain cleavage may be an important mechanism behind photoinduced degradation in OPV and that by-product removal may be effective to regain pre-burn-in efficiency.

RESULTS AND DISCUSSION

Mass and Volume Loss Caused by 290°C Annealing is Consistent with Side Chain Cleavage

Thermogravimetric analysis (TGA) was performed on PTB7 powder to test thermal reactions occurring at high temperature. Results are shown in Figures 2A and 2B and in Figure S1A. Two temperature

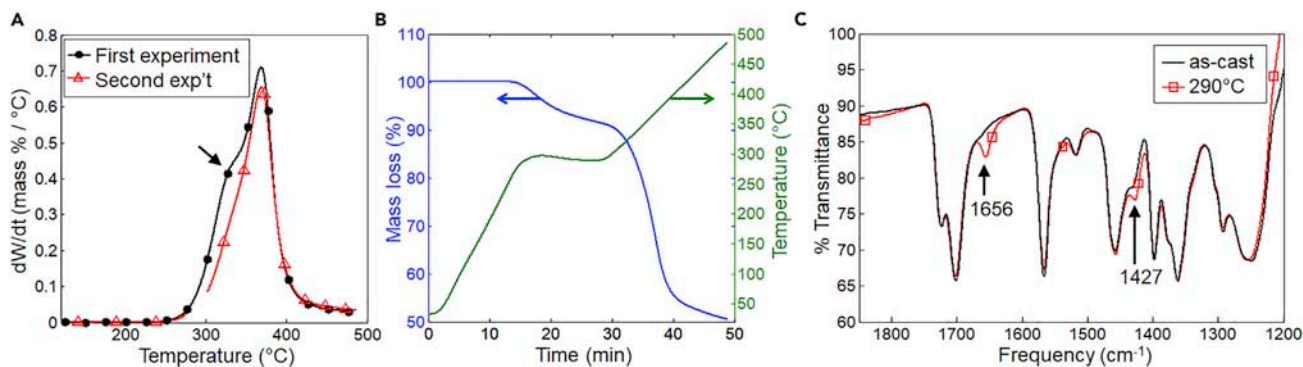


Figure 2. Evidence of a Side Chain Cleavage Reaction at 290°C

(A) Comparison of two TGA experiments: first with a linear ramp and second with temperature held at 290°C for 15 min. The derivative of mass loss is plotted to make mass loss mechanisms easier to distinguish. The first mass loss mechanism (shoulder) marked with an arrow disappears in the second experiment. (B) Mass loss and temperature over time during the second TGA experiment. The mass loss plateaus at about 10% when held at 290°C. (C) FTIR of powder pellet, as received and after 290°C anneal (full spectra shown in Figure S1D). The annealed sample has been shifted and normalized to ease comparison. The frequencies discussed in the text are marked with arrows. See also Figure S1 for (A–C) and Figure S2 for (C).

ramps were performed: the first used a continuous ramp of 10°C/min; the second ramped to 290°C at 20°C/min and held the powder at 290°C for 15 min before continuing to ramp at 10°C/min. The first experiment indicated two mass loss transitions in TGA, evidenced by a peak and a shoulder in the dW/dt curve (Figure 2A). The onset of the first transition was at about 260°C. Since no additional mass loss transitions are observed up to a temperature of 500°C, the second mass loss must represent a final degradation stage wherein the backbone breaks down. In the second ramp, the first mass loss transition (the shoulder) was removed without significantly affecting the second mass loss peak. This indicates that the first mass loss mechanism completes in 15 min at 290°C without initiating the backbone degradation associated with the second mass loss peak. The total mass loss upon completion of the first transition is 10%.

The double transition in TGA is consistent with the previous literature on side-chain-cleavable materials, in which the first TGA mass loss is attributed to side chain cleavage (Guo et al., 2015; Helgesen et al., 2011; Vahdani et al., 2016; Kuhn et al., 2015). Furthermore, the solubility of PTB7 powder dropped significantly after annealing at 290°C, with visible precipitates remaining in a 10-mg/mL solution in chlorobenzene after stirring for several hours at 60°C. Therefore the most likely explanation for the first mass loss mechanism is a side chain cleave, and the plateauing of the mass loss peak after the 290°C anneal indicates that the polymer backbone is not degraded in this process.

Profilometry on annealed films showed a thickness loss of 15% ($\pm 10\%$) after the 290°C anneal (see Figure S1C). This consistency of mass and volume loss indicates that the resultant film does not have a significantly altered density or porosity due to side chain outgassing, which is speculated in the previous literature (Hillebrandt et al., 2016). The high annealing temperature likely allows reorganization of backbones, which closes any pores that might have formed.

The measured mass loss is less than that expected by side chain cleavage. Cleavage on the thiophene ester group would result in a 15% or 21% mass loss depending on the remaining functional group (carboxyl or none). Cleavage of the ether groups on the benzodithiophene result in a mass loss of up to 30% if both side chains are cleaved. The discrepancy in the measured and the expected mass loss, 10% vs 15%–30%, suggests cleavage by-products remaining in the film and/or incomplete side chain cleavage. Since TGA shows completion of the cleavage reaction with these annealing conditions, the mass loss of only 10% indicates that some by-products remain in the film.

FTIR and UV-Vis Changes Support a Cleavage Reaction and Are Similar between Annealing and Irradiation

FTIR spectra were collected on as-received and annealed PTB7 powder to study the changes in chemical structure, and the results are shown in Figure 2C. The most significant change in the FTIR spectra was the

increased absorption at 1,656 and 1,427 cm^{-1} after annealing. To elucidate the source of these changes, we studied FTIR spectra of a series of potential side-chain-removal intermediate compounds from NIST Chemistry WebBook, Standard Reference Database Number 69 (Linstrom and Mallard, 2017). The FTIR of the annealed PTB7 was compared with the FTIR spectra of simple thiophene and benzodithiophene derivatives (reproduced in Figure S2 for ease of comparison).

Peaks at or near 1,656 and 1,427 cm^{-1} are present in FTIR spectra of 5-methyl-2-thiophenecarboxylic acid and 2-thiophenecarboxaldehyde (CAS registry numbers 1918-79-2 and 98-03-3) but not in the FTIR spectrum of 2-thiophenemethanol (636-72-6) or thiophene (110-02-1). In addition, the 1,656 cm^{-1} peak is not present in 2-thiophenecarboxylic acid, ethyl ester (2810-04-0).

This indicates that the structural changes may involve modification or removal of the ester side chain of the thieno[3,4-b]thiophene, resulting in the formation of either a carboxylic acid or an aldehyde group. A similar analysis of a side chain removal reaction on the benzodithiophene indicates that formation of benzoquinone could be responsible for the peak at 1,656 cm^{-1} ; however, this would result in significant changes to the UV-Vis absorbance spectrum (Wilke et al., 2013), which is not observed (see below).

Alternatively, a strong peak at 1,656 cm^{-1} is observed in the FTIR for 2-ethyl-1-hexene (CAS 1632-16-2), which is a potential by-product of a side chain cleavage reaction. This is consistent with side chain cleavage with some by-product trapping.

Thus the most probable cause of the changes in FTIR after annealing is cleavage at the thiophene, removing an 8-carbon segment, with or without a hydroxyl group. It follows that the composition of any by-product of this reaction must be some configuration of $\text{C}_8\text{H}_{17}\text{OH}$ or fragments thereof.

The optical properties were analyzed using UV-Vis spectroscopy, shown in Figure 4C. The spectra are shown as absorption coefficient (see Supplemental Information for details). The main features in the spectra are overlapping absorptions at approximately 628 and 676 nm, which we assign to the 0-1 and 0-0 levels of the π - π^* transition, respectively.

Annealing the film to 120°C and 260°C showed a gradual redshift in absorption, which can be attributed to an increase in the planarity of the polymer backbone, leading to an increase in the extent of electron delocalization, or conjugation length (Li et al., 2005). The shape of the absorption was approximately unchanged on annealing to 120°C and 260°C.

Annealing at 290°C resulted in a noticeable blueshift in the absorption position relative to the films annealed at 260°C, accompanied by a reduction in the absorption primarily at higher wavelengths (i.e., 0-0 level) and an increase in the width. These changes suggest that the film becomes more disordered and that the conjugation length decreases (Li et al., 2005; Kim and Swager, 2001; Bencheikh et al., 2015; Barford and Marcus, 2017). Previous work shows that blueshift in UV-Vis spectra can be associated with decreasing side chain bulkiness (Naik et al., 2012), so this also supports a side chain cleavage reaction. What is not observed is the drastic change in the absorbance spectra that would result from decomposition of the conjugated π -system (backbone).

Both FTIR and UV-Vis changes seen here are remarkably similar to changes observed in PTB7 films after UV irradiation in air (Son et al., 2011). Here, a photochemical reaction on the thiophene, which does not destroy the conjugation, is responsible for the loss in device efficiency. This similarity of changes in FTIR and UV-Vis indicates that the same reaction that we observe under high-temperature annealing may also occur under irradiation in air. Namely, side chain cleavage may be an important mechanism in photoinduced degradation in PTB7, with reaction by-products leading to efficiency loss. A comparison of FTIR and UV-Vis from as-cast, annealed, and irradiated samples is shown in Figures S1B and S3, respectively, and confirms that the opto-electronic changes during annealing (at 290°C) are similar to those arising from solar irradiation in air, suggesting that high-temperature annealing and irradiation result in the same decomposition product produced via side chain cleavage. Furthermore, the film that has been annealed at 290°C and then irradiated shows a UV-Vis spectrum nearly identical to that of the annealed sample (see Figure S3), suggesting that annealing stabilizes the film toward further degradation. This is consistent with increased stability after side chain cleavage seen in the literature (Manceau et al., 2010; Helgesen et al., 2011).

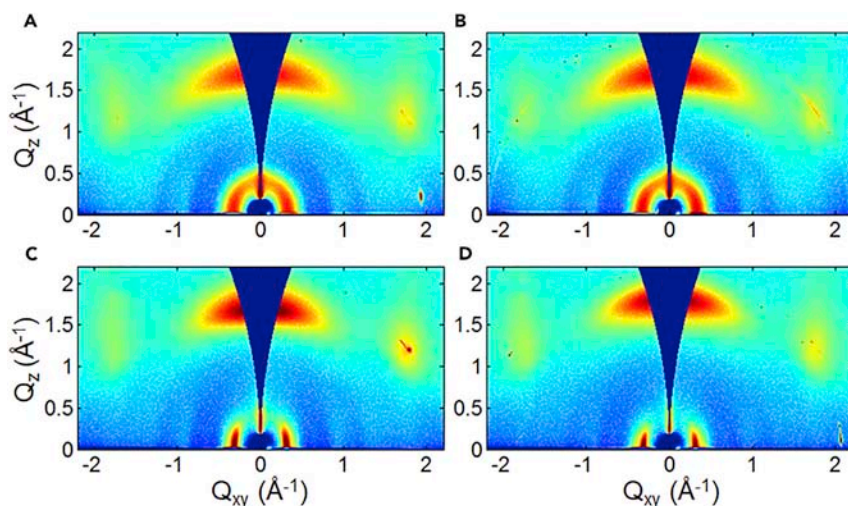


Figure 3. 2D Scattering Pattern for Neat PTB7 Films

(A–D) (A) as-cast, (B) 120°C anneal, (C) 260°C anneal, and (D) 290°C anneal. Images are plotted with intensity (detector counts) on a logarithmic scale, using the same color scaling for all images. Each image represents a 10-min exposure. The yellow spots at $Q_{xy} \approx 1.9$, $Q_z \approx 1.2 \text{ \AA}^{-1}$ are diffuse scattering from the silicon substrate. See also Figures S4 and S5.

Annealing Results in a Decrease in Morphological Disorder and a Closer Packing Motif

Grazing Incidence Wide Angle X-ray Scattering (GIWAXS) was measured on neat PTB7 films to analyze the morphological changes occurring after increasing the polymer chain mobility (heating up to 260°C) and after cleavage of the side chains (heating to 290°C). The GIWAXS detector images for four neat PTB7 films with different annealing temperatures—as-cast, 120°C, 260°C, and 290°C—are shown in Figures 3A–3D, and the integrated 1D spectra are shown in Figure 4A (in-plane) and Figure 4B (out-of-plane). The as-cast image shows scattering peaks at approximately $Q = 0.33 \text{ \AA}^{-1}$ primarily in the in-plane direction (along Q_{xy}) and at $Q = 1.7 \text{ \AA}^{-1}$ in the out-of-plane direction (along Q_z). These peaks correspond to an alkyl side chain spacing of 19 Å and a π - π stacking distance of 3.7 Å, respectively (Prosa et al., 1992). The orientation of these peaks shows a face-on configuration, illustrated in Figure 1B, consistent with previous measurements of PTB7 (Hammond et al., 2011; Tang and McNeill, 2013; Das et al., 2015).

Data from the sample annealed to 120°C shows good agreement with those from the as-cast sample. In contrast, the 260°C annealed sample shows a decrease in peak width along Q from the as-cast sample. After the 260°C anneal, the peak at $Q = 0.33 \text{ \AA}^{-1}$ splits into two overlapping peaks (or, a peak plus a shoulder). The broad alkyl peak in the as-cast sample is at an intermediate position between the overlapping peaks in the annealed sample, so it is reasonable to assume that both peaks are present but not resolvable in the as-cast material. The stronger of these peaks can be attributed to alkyl stacking, but the source of the second peak is not immediately clear. It is possible that this peak is due to the spacing along the polymer backbone. The peak position corresponds to a spacing of about 16 Å (see Figure S5), which is close to the expected monomer length in PTB7.

In addition to the decrease in peak width, a decrease in the angular width of both the alkyl stacking peak and the π - π stacking peak after annealing to 260°C is noticeable in the pole figures (Figure S4). These observations show a significant decrease in disorder and increase in the degree of orientation in the polymer, which is consistent with the effects of annealing found for other polymers (Ruderer and Muller-Buschbaum, 2011). The decrease in disorder is also consistent with the redshift seen in the UV-Vis spectra.

Annealing to 290°C gave an in-plane scattering pattern similar to that of the 260°C annealed sample. Remarkably, however, the 290°C annealed sample showed a shift in the π - π stacking peak from $Q = 1.69 \text{ \AA}^{-1}$ to $Q = 1.80 \text{ \AA}^{-1}$, or from $d = 3.73 \text{ \AA}$ to $d = 3.49 \text{ \AA}$ (Table S1). This 6% decrease in the π - π stacking distance represents a closer packing structure previously unseen in PTB7. This finding is consistent with the removal of side chains, as steric interactions between side chains can push polymer backbones apart to larger π - π stacking distances, especially for branched side chains (Lei et al., 2014; Oosterhout et al., 2017).

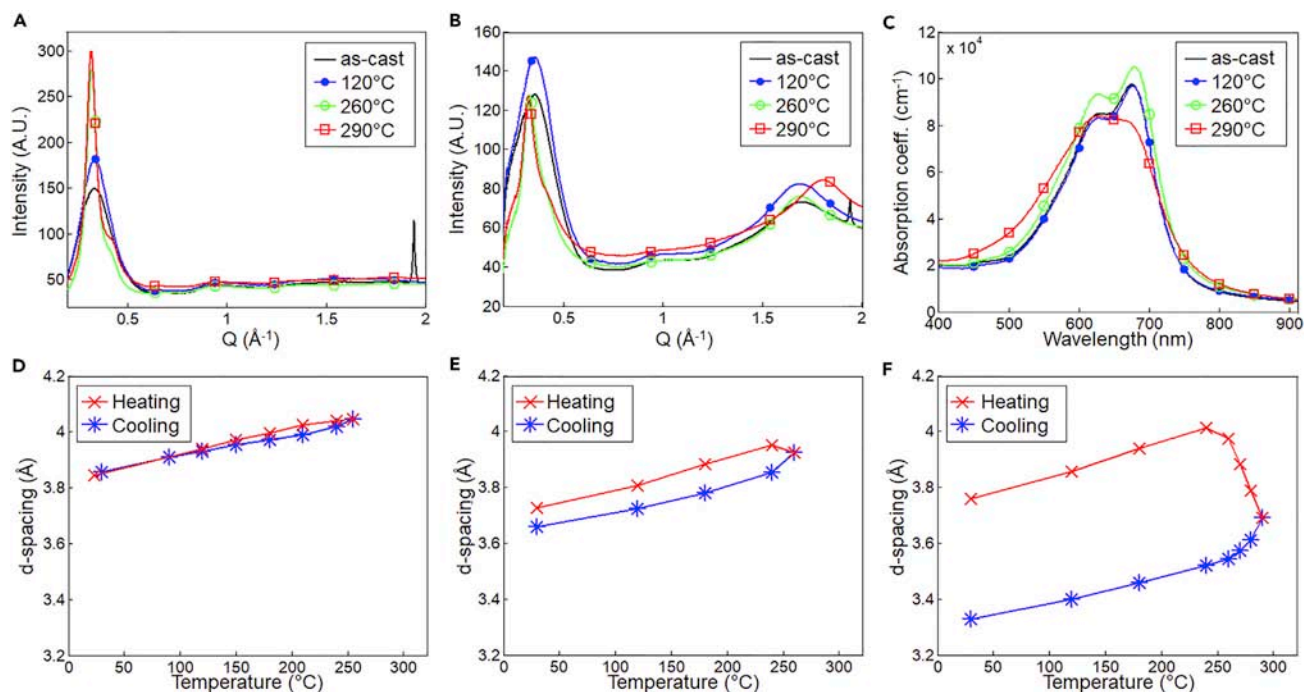


Figure 4. Changes to Neat PTB7 Films with Different Annealing Temperatures

(A) In-plane integration of GIWAXS patterns in Figure 3 between $\chi = 5^\circ$ – 20° (and 160° – 175°), after χ -correction (see Supplemental Information for details). (B) Out-of-plane integration of GIWAXS between $\chi = 75^\circ$ – 105° . (C) UV-Vis absorption spectra of neat PTB7 films. (D–F) d-Spacing of the π - π stacking peak during *in situ* heating to 255°C (D), 260°C (E), and 290°C (F). For clarity, measurements during heating and cooling are shown in red and blue, respectively. It should be noted that the sample in (D) was measured with an older PTB7 batch, GIWAXS setup, and calibration procedure than (E) and (F), which explains the slightly different initial d-spacing. See also Figures S4 and S5 for (A and B), Figure S3 for (C), and Figure S6 for (D–F).

The UV-Vis showed an increase in opto-electronic disorder when the annealing temperature was increased from 260°C to 290°C, whereas GIWAXS showed similar peak intensities and orientations for the 260°C and the 290°C annealed samples. Thus changes in the opto-electronic properties are not correlated directly with changes in morphology as observed with X-ray diffraction. This suggests that by-products in the film created by side chain cleavage cause the observed changes in opto-electronic structure (e.g., form traps) without affecting the polymer packing.

An *in situ* annealing study was performed to track the dynamics of morphological changes. In-plane and out-of-plane integrated curves for *in situ* GIWAXS experiments are shown in Figure S6. The first as-cast sample was gradually heated to 255°C and cooled to room temperature while measuring GIWAXS in a 4-hr procedure. The π - π stacking peak shifted to higher d-spacing upon heating and reversibly shifted back during cooling as shown in Figure 4D, which is due to thermal expansion and contraction.

The second sample was gradually heated to 260°C and cooled during a 2-hr procedure (Figure 4E), and the third sample was gradually heated to 290°C and cooled during a 4-hr procedure (Figure 4F). The π - π stacking distance decreased irreversibly while the temperature was above an onset temperature of about 260°C and otherwise followed thermal expansion and contraction trends. Post 290°C anneal, a decrease in π - π stacking distance of 11% was observed. These data show that the decrease in the π - π stacking distance can be associated with the side chain cleavage that occurs above 260°C. The larger change in the distance of the *in situ* annealed films (11% for *in situ* versus 6% for *ex situ*) is likely due to the film being held at high temperatures for a longer time period during *in situ* annealing, allowing a more complete reaction.

The linear coefficient of thermal expansion (CTE) was calculated to be $3.6 \times 10^{-4}/^\circ\text{C}$ for the sample annealed to 255°C, 2.9 and $2.5 \times 10^{-4}/^\circ\text{C}$ for the sample annealed to 260°C (for heating and cooling,

Processing Temp (°C)	Hole Mobility: (cm ² /Vs)
As-cast	(2.85 ± 1.3) × 10 ⁻⁴
120°C	(4.7 ± 0.9) × 10 ⁻⁴
260°C	(10.5 ± 1) × 10 ⁻⁴
290°C	(0.82 ± 0.55) × 10 ⁻⁴

Table 1. Hole Mobility of Neat PTB7 Films, Measured Using SCLC

Each value is the average mobility for eight devices and ± error is the standard deviation. See also Figure S8.

respectively), and 3.2 and 2.7 × 10⁻⁴/°C for the sample annealed to 290°C. These values are consistent to within a factor of two of CTE estimated for the lamella spacing of a thin film of P3HT (~4.8 × 10⁻⁴/°C) (Verploegen et al., 2010).

In situ annealed samples were cooled slowly, unlike *ex situ* annealed samples, which were quenched (details in Supplemental Information). The previous literature for P3HT:PCBM has shown that rapid quenching can result in non-equilibrium morphological states (Wang et al., 2011). The consistency of the morphology change in quenched and gradually cooled samples indicates that the closer packing motif is not a kinetically trapped state but is nearly energetically stable.

Mobility Decreases due to Side Chain Cleavage

The as-cast and annealed neat PTB7 films were further analyzed using space charge limited current (SCLC) measurements. This technique measures charge transport mobility in the out-of-plane direction, which is most influenced by hopping in the π-π stacking direction of this face-on polymer. The device schematic used is shown in Figure S8A, and resulting J-V curves are shown in Figure S8B. Hole mobility was calculated from SCLC measurements using the Mott-Gurney equation:

$$J = \frac{9}{8} \epsilon_0 \epsilon_r \mu \frac{V^2}{L^3}$$

where J is the current density, V is the applied effective voltage, L is the thickness of the active layer, ε₀ is the absolute permittivity, ε_r is the relative permittivity (taken as 3), and μ is the hole mobility (Lampert and Mark, 1970; Blakesley et al., 2014). To confirm the reliability of the SCLC measurement, the thickness dependence of J (J ∝ L⁻³) was shown to be consistent with the Mott-Gurney equation (Figure S8C).

The hole mobility of the PTB7 measured as a function of annealing temperature is shown in Table 1. Each result shown is from an average of eight devices. The room temperature mobility of as-cast PTB7 was within the mobility range found in the literature using SCLC (Foster et al., 2014; Liang et al., 2010; Zhou et al., 2014). The mobility increased significantly from the as-cast device to the 120°C annealed device and from the 120°C annealed device to the 260°C annealed device (~2–3 times). Thus an increase in mobility accompanies the increase in conjugation length and decrease in morphological disorder, and this can be achieved through moderate-temperature annealing. This supports the picture in semiconducting polymers that increased order within the same polymer leads to higher mobility.

Conversely, the mobility fell by over an order of magnitude after annealing to 290°C, consistent with the higher electronic disorder seen in UV-Vis. Previous work has also reported that a decrease in π-π spacing does not always correlate with increased mobility; however, this work instigates an unfavorable change in polymer crystallinity (Dou et al., 2014), which we do not observe in GIWAXS. Our result is significant, as it shows that an improved morphology (decrease in disorder and decrease in π-π spacing) and favorable removal of insulating side chains may come with complex adverse side effects, leading to an overall decrease in electronic performance.

We speculate that two factors may contribute. The first is that by-products of the side chain cleavage reaction cause an increase in electronic disorder that leads to a decrease in mobility. The second is the possibility of carrier trapping at the post-cleavage functional group such as proton transfer at a carboxylic acid.

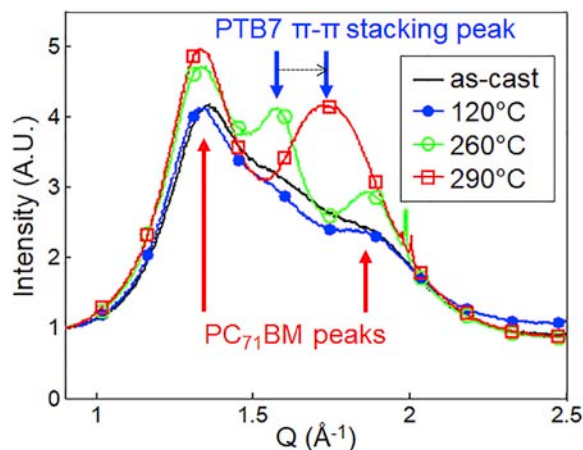


Figure 5. Changes in GIWAXS Patterns of Blend PTB7:PC₇₁BM Films with Different Annealing Temperatures

Integrated out-of-plane cake slice (75°–105°) from Figure S7 in the region of the π - π stacking peak, with arrows showing positions of PC₇₁BM and PTB7 peaks. Arbitrary normalization.

See also Figure S7.

The Effect of Annealing on PTB7:PC₇₁BM Blend Films is Consistent with that on Neat PTB7

We have shown that neat PTB7 films become better ordered with annealing and undergo a side chain cleavage reaction above 260°C, which decreases intermolecular spacing. In this section, we show that these morphological changes are also observed in PTB7:PC₇₁BM blends. Furthermore, the mobility of neat PTB7 decreases significantly post cleavage, which we attribute to the inclusion of reaction by-products. Here, we give evidence for the existence of trapped by-products by observing faster decay of time-resolved photoluminescence in PTB7:PC₇₁BM blends. This shows that our findings can be applied to BHJ-based devices. BHJ films were spin cast from a PTB7:PC₇₁BM 1:1.5 ratio in chlorobenzene with a total solids concentration of 10 mg/mL.

First, we examine GIWAXS results for blend films, shown in Figure S7. Accurate quantitative analysis of blend data is complicated by the overlap between PC₇₁BM peaks at ~ 1.3 and 1.9 \AA^{-1} and the PTB7 π - π stacking peak at $\sim 1.6 \text{ \AA}^{-1}$. However, changes to the GIWAXS patterns are clearly visible in the out-of-plane integrated image in Figure 5. Here, annealing to 120°C gives a pattern similar to that of the as-cast film, whereas annealing to 260°C gives a distinct sharpening of the PTB7 π - π stacking peak. This behavior is identical to that observed in neat PTB7 films. Furthermore, annealing the BHJ to 290°C causes the PTB7 π - π stacking peak to shift to a higher Q, with the peak shifting from approximately $Q = 1.57$ to $Q = 1.75 \text{ \AA}^{-1}$ ($d = 4.00$ to 3.59 \AA). This is a change of about 11%, consistent with the neat film. However, the PTB7 π - π stacking peak overlaps strongly with the PC₇₁BM peaks at 1.3 and 1.9 \AA^{-1} , making determination of the π - π peak position inaccurate and explaining the slight difference with Figure 4 (neat film data). These results show that PTB7 morphology behaves similarly in blend films as in neat films and that mixing with a fullerene does not hinder the side chain cleavage reaction presented here.

With GIWAXS results indicating a closer packing arrangement due to side chain cleavage, we next examine how cleavage by-products affect the blend films compared with neat films. Side chain cleavage by-products may act as recombination sites, resulting in faster exciton quenching in PC₇₁BM blends. This was studied using time-resolved photoluminescence (TR-PL), with a 515 nm excitation and emission in the range 670–720 nm. In previous work with a 400 nm excitation, photoluminescence from PTB7 was quenched very quickly in this blend, so only PC₇₁BM emission was detected using this method (Hedley et al., 2017). In the present work the detection wavelength range selects for emission from PC₇₁BM. The emission had two components: a fast component, which occurs on a timescale of several picoseconds, and a slow component ($> \sim 10$ picoseconds). Previous work indicates that fast quenching may be due to hole transfer or resonant energy transfer from the fullerene to the polymer in intimately mixed polymer:fullerene regions, in which the sizes of PC₇₁BM domains are less than 10 nm. Thus the degree of fast quenching (proportional to the change in PL in the first few picoseconds after excitation) loosely corresponds to the amount of small PC₇₁BM domains, and domain growth will lead to less quenching on a fast timescale.

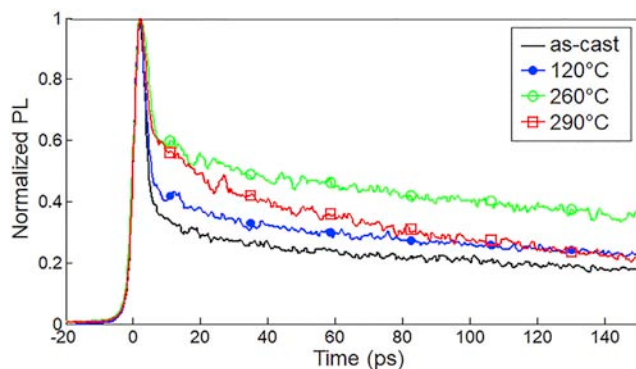


Figure 6. TR-PL Data from Blend Films As-cast and Annealed to 120°C, 260°C, and 290°C

Data have been normalized by the maximum luminescence at 0 ps and smoothed for visibility.

The slow component of quenching results from quenching at the polymer:fullerene interface after exciton diffusion from within larger PC₇₁BM domains. The diffusion distance increases with increasing domain size and increasing domain purity. Including even a small amount of impurity in a fullerene domain (e.g., 0.2 weight % PTB7) has been shown to significantly increase the rate of quenching, corresponding to a faster time constant in the TR-PL curve (Hedley et al., 2017).

TR-PL data from PTB7:PC₇₁BM films annealed to various temperatures are shown in Figure 6. From the ratio of maximum luminescence to luminescence after 10 ps, we can see a decrease in the fast-timescale quenching from the as-cast film to 120°C, and from 120°C to 260°C. This is consistent with the increased phase separation in PTB7-Th:PC₆₀BM observed in previous work: the level of mixing decreases and domain sizes increase with annealing (Hsieh et al., 2017). Notably, the 260°C- and 290°C-annealed BHJ films show similar amounts of fast-timescale quenching, which may be due to the film reaching a stable morphology. A saturation of thermally induced intermixing has been observed in PTB7:PC₆₀BM previously (Liu et al., 2014), and so it is not unexpected that an equilibrium may be reached.

The slow-timescale quenching, in contrast, is fairly similar between as-cast, 120°C, and 260°C annealed films, but becomes substantially faster after annealing at 290°C. Because the fast-timescale quenching is similar between 260°C and 290°C, this is most likely due to the existence of trap states in PC₇₁BM domains that are created by the cleavage reaction. This would arise if some of the cleavage products, which have low molecular weight and are therefore mobile in a hot film, diffuse into the fullerene domains and quench the PL. It supports our conjecture that cleavage by-products remain in the film, disrupting mobility and exciton diffusion by acting as trap states.

GIWAXS and TR-PL on BHJ films show that annealing effects are similar in neat and blend films. Up to 260°C, PTB7 becomes better ordered and more segregated from PC₇₁BM. Above 260°C, a side chain cleavage reaction occurs, which decreases the π - π stacking distance of PTB7 and results in by-product trap states in both the neat PTB7 and in PC₇₁BM-rich domains of the blend.

Conclusions

In this work, we have shown that moderate-temperature annealing leads to an improvement in film morphology and a 2–3x increase in hole mobility. High-temperature annealing leads to a side chain cleavage reaction in PTB7, which coincides with a decrease in intermolecular distance, both in neat and PC₇₁BM blend films. These results are important for organic electronics because the removal of insulating side chains and decrease in intermolecular distance are expected to improve device efficiency. However, the presence of reaction by-products, likely composed of C₈H₁₇OH and/or fragments thereof, leads instead to a decrease in mobility and faster decay of the PL. The similarity between thermally cleaved films and irradiated films leads us to suggest that side chain cleavage is a mechanism responsible for burn-in.

The results presented here show that thermally induced side chain cleavage is possible in high-performing materials without additional structural modification and that this cleavage process can lead to favorable

changes in molecular packing. Although the cleavage temperature used here is too high to be a viable processing step for flexible substrates used in OPV, previous work suggests that reduction of cleavage temperature can be achieved through the inclusion of a catalyst (Vahdani et al., 2016) or by appropriately engineered side chains (Hillebrandt et al., 2016). Additional processing steps may be developed to target and remove trap states formed in this reaction, and the decrease of solubility of the polymer backbones without side chains can aid this process. For example, the polymer matrix may be swelled using an appropriate solvent wash, allowing the release of volatile hydrocarbon by-products. The correlation of side chain cleavage with photoinduced degradation indicates that these same washing procedures may be used to remove the damaging sub-gap trap states that form during burn-in.

METHODS

All methods can be found in the accompanying [Transparent Methods supplemental file](#).

SUPPLEMENTAL INFORMATION

Supplemental Information includes Transparent Methods, eight figures, and two tables and can be found with this article online at <https://doi.org/10.1016/j.isci.2018.03.002>.

ACKNOWLEDGMENTS

This work was supported by the Office of Naval Research NDSEG fellowship (V.S.) and the Department of Energy SCGSR Program (L.J.P.). Work was partially supported by the Department of the Navy, Office of Naval Research Award No. N00014-14-1-0580 (S.D.O., M.F.T.). L.K.J., I.R., and I.D.W.S. were supported by the Engineering and Physical Sciences Research Council (grants EP/L017008/1 and EP/L012294/1). I.D.W.S. also acknowledges support from a Royal Society Wolfson Research Merit Award. Use of the Stanford Synchrotron Radiation Lightsource, SLAC National Accelerator Laboratory, is supported by the U.S. Department of Energy, Office of Science, Office of Basic Energy Sciences under Contract No. DE-AC02-76SF00515. We would like to thank Ging-ji Nathan Wong and Jeffery Tok for help with various experiments. Part of this work was performed at the Stanford Nano Shared Facilities (SNSF), supported by the National Science Foundation under award ECCS-1542152. We would like to thank M.T. Sajjad and A. Ruseckas for assistance with the time-resolved PL measurements. We would also like to thank Chris Takacs for helpful discussions.

AUTHOR CONTRIBUTIONS

Conceptualization, V.S., L.K.J., I.D.W.S., and M.F.T.; Methodology, V.S., L.K.J., I.R., I.D.W.S., and M.F.T.; Validation, V.S. and L.K.J.; Formal Analysis, V.S. and L.K.J.; Investigation, V.S., L.K.J., L.J.P., S.D.O., C.J.D., and I.R.; Writing – Original Draft, V.S., L.K.J.; Writing – Review and Editing, all authors; Visualization, V.S. and L.K.J.; Supervision, I.D.W.S. and M.F.T.; Funding Acquisition, V.S., I.D.W.S., C.J.D., and M.F.T.

DECLARATION OF INTERESTS

The authors declare no competing interests.

Received: March 1, 2017

Revised: February 5, 2018

Accepted: February 16, 2018

Published: March 22, 2018

REFERENCES

- Barford, W., and Marcus, M. (2017). Perspective: optical spectroscopy in π -conjugated polymers and how it can be used to determine multiscale polymer structures. *J. Chem. Phys.* 146, 130902.
- Bencheikh, F., Duché, D., Ruiz, C.M., Simon, J.-J., and Escoubas, L. (2015). Study of optical properties and molecular aggregation of conjugated low band gap copolymers: PTB7 and PTB7-Th. *J. Phys. Chem. C* 119, 24643–24648.
- Blakesley, J.C., Castro, F.A., Kylberg, W., Dibb, G.F.A., Arantes, C., Valaski, R., Cremona, M., Kim, J.S., and Kim, J.-S. (2014). Towards reliable charge-mobility benchmark measurements for organic semiconductors. *Org. Electron.* 15, 1263–1272.
- BP (2016). BP Statistical Review of World Energy 2016 (BP Distribution Services).
- Coropceanu, V., Cornil, J., Filho, D.A., Olivier, Y., Silbey, R., and Bredas, J.-L. (2007). Charge transport in organic semiconductors. *Chem. Rev.* 107, 926–952.
- Das, S., Keum, J.K., Browning, J.F., Gu, G., Yang, B., Dyck, O., Do, C., Chen, W., Chen, J., Ivanov, I.N., et al. (2015). Correlating high power conversion efficiency of PTB7:PC71BM inverted organic solar cells with nanoscale structures. *Nanoscale* 7, 15576–15583.
- Dkhil, S.B., Pfannmöller, M., Saba, M.I., Gaceur, M., Heidari, H., Videlot-Ackermann, C., Margeat,

- O., Guerrero, A., Bisquert, J., Garcia-Belmonte, G., et al. (2017). Toward high-temperature stability of PTB7-based bulk heterojunction solar cells: impact of fullerene size and solvent additive. *Adv. Energy Mater.* 7, 1601486.
- Dou, J.-H., Zheng, Y.-Q., Lei, T., Zhang, S.-D., Wang, Z., Zhang, W.-B., Wang, J.-Y., and Pei, J. (2014). Systematic investigation of side-chain branching position effect on electron carrier mobility in conjugated polymers. *Adv. Funct. Mater.* 24, 6270–6278.
- Foster, S., Deledalle, F., Mitani, A., Kimura, T., Kim, K.-B., Okachi, T., Kirchartz, T., Oguma, J., Miyake, K., Durrant, J.R., et al. (2014). Electron collection as a limit to polymer:PCBM solar cell efficiency: effect of blend microstructure on carrier mobility and device performance in PTB7:PCBM. *Adv. Energy Mater.* 4, 1400311.
- Guo, C., Quinn, J., Sun, B., and Li, Y. (2015). An indigo-based polymer bearing thermocleavable side chains for n-type organic thin film transistors. *J. Mater. Chem. C.* 3, 5226–5232.
- Hammond, M.R., Kline, R.J., Herzing, A.A., Richter, L.J., Germack, D.S., Ro, H.-W., Soles, C.L., Fischer, D.A., Xu, T., Yu, L., et al. (2011). Molecular order in high-efficiency polymer/fullerene bulk heterojunction solar cells. *ACS Nano* 5, 8248–8257.
- Hedley, G.J., Ruseckas, A., and Samuel, I.D.W. (2017). Light harvesting for organic photovoltaic. *Chem. Rev.* 117, 796–837.
- Helgesen, M., Madsen, M.V., Andreasen, B., Tromholt, T., Andreasen, J.W., and Krebs, F.C. (2011). Thermally reactive Thiazolo[5,4-d]thiazole based copolymers for high photochemical stability in polymer solar cells. *Polym. Chem.* 2, 2536–2542.
- He, Z., Xiao, B., Liu, F., Wu, H., Yang, Y., Xiao, S., Wang, C., Russell, T.P., and Cao, Y. (2015). Single-junction polymer solar cells with high efficiency and photovoltage. *Nat. Photonics* 9, 174–179.
- Hillebrandt, S., Adermann, T., Alt, M., Schinke, J., Glaser, T., Mankel, E., Hernandez-Sosa, G., Jaegermann, W., Lemmer, U., Pucci, A., et al. (2016). Naphthalene tetracarboxydiimide-based n-type polymers with removable solubility via thermally cleavable side chains. *ACS Appl. Mater. Interfaces* 8, 4940–4945.
- Höfle, S., Zhang, M., Dlugosch, J., Kuhn, M., Hamburger, M., and Colmann, A. (2017). Thermo-cleavable poly(fluorene-benzothiadiazole) to enable solution deposition of multi-layer organic light emitting diodes. *Org. Electron.* 42, 355–360.
- Hsieh, Y.-J., Huang, Y.-C., Liu, W.-S., Su, Y.-A., Tsao, C.-S., Rwei, S.-P., and Wang, L. (2017). Insights into the morphological instability of bulk heterojunction PTB7-Th/PCBM solar cells upon high-temperature aging. *ACS Appl. Mater. Interfaces* 9, 14808–14816.
- Kim, J., and Swager, T.M. (2001). Control of conformational and interpolymer effects in conjugated polymers. *Nature* 411, 1030–1034.
- Kuhn, M., Ludwig, J., Marszalek, T., Adermann, T., Pisula, W., Müllen, K., Colmann, A., and Hamburger, M. (2015). Tertiary carbonate side chains: easily tunable thermo-labile breaking points for controlling the solubility of conjugated polymers. *Chem. Mater.* 27, 2678–2686.
- Kymissis, I. (2009). *Organic Field Effect Transistors*, First Edition (Springer US).
- Lampert, M.A., and Mark, P. (1970). Semiconductor technique. (Book reviews: current injection in solids). *Science* 170, 966–967.
- Lei, T., Wang, J.-Y., and Pei, J. (2014). Design, synthesis, and structure–property relationships of isoindigo-based conjugated polymers. *Acc. Chem. Res.* 47, 1117–1126.
- Liang, Y., Xu, Z., Xia, J., Tsai, S.-T., Wu, Y., Li, G., Ray, C., and Yu, L. (2010). For the bright future—bulk heterojunction polymer solar cells with power conversion efficiency of 7.4%. *Adv. Mater.* 22, E135–E138.
- Li, G., Shrotriya, V., Huang, J., Yao, Y., Moriarty, T., Emery, K., and Yang, Y. (2005). High-efficiency solution processable polymer photovoltaic cells by self-organization of polymer blends. *Nat. Mater.* 4, 864–868.
- Linstrom, P.J., and Mallard, W.G. (2017). NIST Chemistry WebBook, NIST Standard Reference Database Number 69 (National Institute of Standards and Technology).
- Liu, F., Zhao, W., Tumbleston, J.R., Wang, C., Gu, Y., Wang, D., Briseno, A.L., Ade, H., and Russell, T.P. (2014). Understanding the morphology of PTB7:PCBM blends in organic photovoltaics. *Adv. Energy Mater.* 4, 1301377.
- Manceau, M., Helgesen, M., and Krebs, F.C. (2010). Thermo-cleavable polymers: materials with enhanced photochemical stability. *Polym. Degrad. Stab.* 95, 2666–2669.
- Mateker, W.R., and McGehee, M.D. (2017). Progress in understanding degradation mechanisms and improving stability in organic photovoltaics. *Adv. Mater.* 29, 1603940.
- Naik, M.A., Venkatramaiah, N., Kanimozhi, C., and Patil, S. (2012). Influence of side-chain on structural order and photophysical properties in thiophene based diketopyrrolopyrroles: a systematic study. *J. Phys. Chem. C* 116, 26128–26137.
- Oosterhout, S.D., Braunecker, W.A., Owczarczyk, Z.R., Ayzner, A.L., Toney, M.F., Olson, D.C., and Kopidakis, N. (2017). Molecular engineering to improve carrier lifetimes for organic photovoltaic devices with thick active layers. *Org. Electron.* 47, 57–65.
- Prosa, T.J., Winokur, M.J., Moulton, J., Smith, P., and Heeger, A.J. (1992). X-ray structural studies of poly(3-alkylthiophenes): an example of an inverse comb. *Macromolecules* 25, 4364–4372.
- Ruderer, M.A., and Müller-Buschbaum, P. (2011). Morphology of polymer-based bulk heterojunction films for organic photovoltaics. *Soft Matter* 7, 5482–5493.
- Son, H.J., Wang, W., Xu, T., Liang, Y., Wu, Y., Li, G., and Yu, L. (2011). Synthesis of fluorinated polythienothiophene-co-benzodithiophenes and effect of fluorination on the photovoltaic properties. *J. Am. Chem. Soc.* 133, 1885–1894.
- Sun, B., Hong, W., Aziz, H., and Li, Y. (2012). Diketopyrrolopyrrole-based semiconducting polymer bearing thermocleavable side chains. *J. Mater. Chem.* 22, 18950–18955.
- Tang, Y., and McNeill, C.R. (2013). All-polymer solar cells utilizing low band gap polymers as donor and acceptor. *J. Polym. Sci. B Polym. Phys.* 51, 403–409.
- Upama, M.B., Wright, M., Puthen-Veetil, B., Elumalai, N.K., Mahmud, M.A., Wang, D., Chan, K.H., Xu, C., Haque, F., and Uddin, A. (2016). Analysis of burn-in photo degradation in low bandgap polymer PTB7 using photothermal deflection spectroscopy. *RSC Adv.* 6, 103899–103904.
- Vahdani, P., Li, X., Zhang, C., Holdcroft, S., and Frisken, B.J. (2016). Morphological characterization of a new low-bandgap thermocleavable polymer showing stable photovoltaic properties. *J. Mater. Chem. A.* 4, 10650–10658.
- Verploegen, E., Mondal, R., Bettinger, C.J., Sok, S., Toney, M.F., and Bao, Z. (2010). Effects of thermal annealing upon the morphology of polymer–fullerene blends. *Adv. Funct. Mater.* 20, 3519–3529.
- Vogelbaum, H.S., and Sauvé, G. (2017). Recently developed high-efficiency organic photoactive materials for printable photovoltaic cells: a mini review. *Synth. Met.* 223, 107–121.
- Wang, T., Pearson, A.J., Lidzey, D.G., and Jones, R.A.L. (2011). Evolution of structure, optoelectronic properties, and device performance of polythiophene:fullerene solar cells during thermal annealing. *Adv. Funct. Mater.* 21, 1383–1390.
- Wilke, T., Schneider, M., and Kleinermanns, K. (2013). 1,4-Hydroquinone is a hydrogen reservoir for fuel cells and recyclable via photocatalytic water splitting. *Open J. Phys. Chem.* 3, 97–102.
- Zhou, N., Lin, H., Lou, S.J., Yu, X., Guo, P., Manley, E.F., Loser, S., Hartnett, P., Huang, H., Wasielewski, M.R., et al. (2014). Morphology-performance relationships in high-efficiency all-polymer solar cells. *Adv. Energy Mater.* 4, 1300785.

ISCI, Volume 2

Supplemental Information

**Morphological, Chemical, and Electronic
Changes of the Conjugated Polymer PTB7
with Thermal Annealing**

Victoria Savikhin, Lethy K. Jagadamma, Lafe J. Purvis, Iain Robertson, Stefan D. Oosterhout, Christopher J. Douglas, Ifor D.W. Samuel, and Michael F. Toney

Supplemental Figures

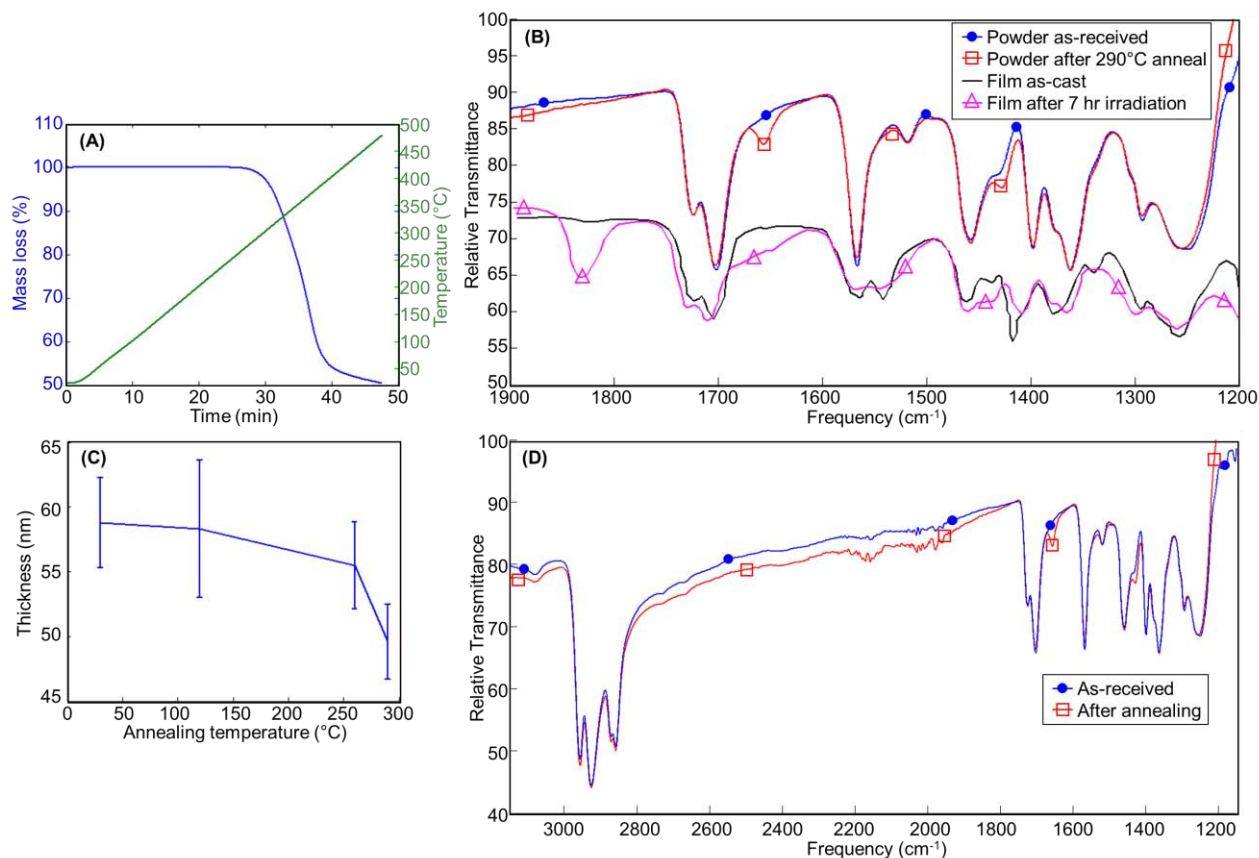


Figure S1. (A) TGA curve with linear temperature ramp. (B) Zoom-in of FT-IR of powder (two top curves) compared to data on photoinduced degradation digitized and reproduced from (Son, *et al.*, 2011) with permission (bottom two curves). The most significant change in our data upon annealing is at 1656 cm⁻¹; (Son, *et al.*, 2011) discusses changes around 1656 cm⁻¹ as the most significant result of irradiation. Differences between our data and the literature may be due to batch variation. (C) Thickness measured with profilometry with error bars indicating \pm one standard deviation. (D) Complete FT-IR curve (subset shown in Figure 2c). (A) and (C) are related to Figure 2 (A,B); (B) and (D) are related to Figure 2 (C).

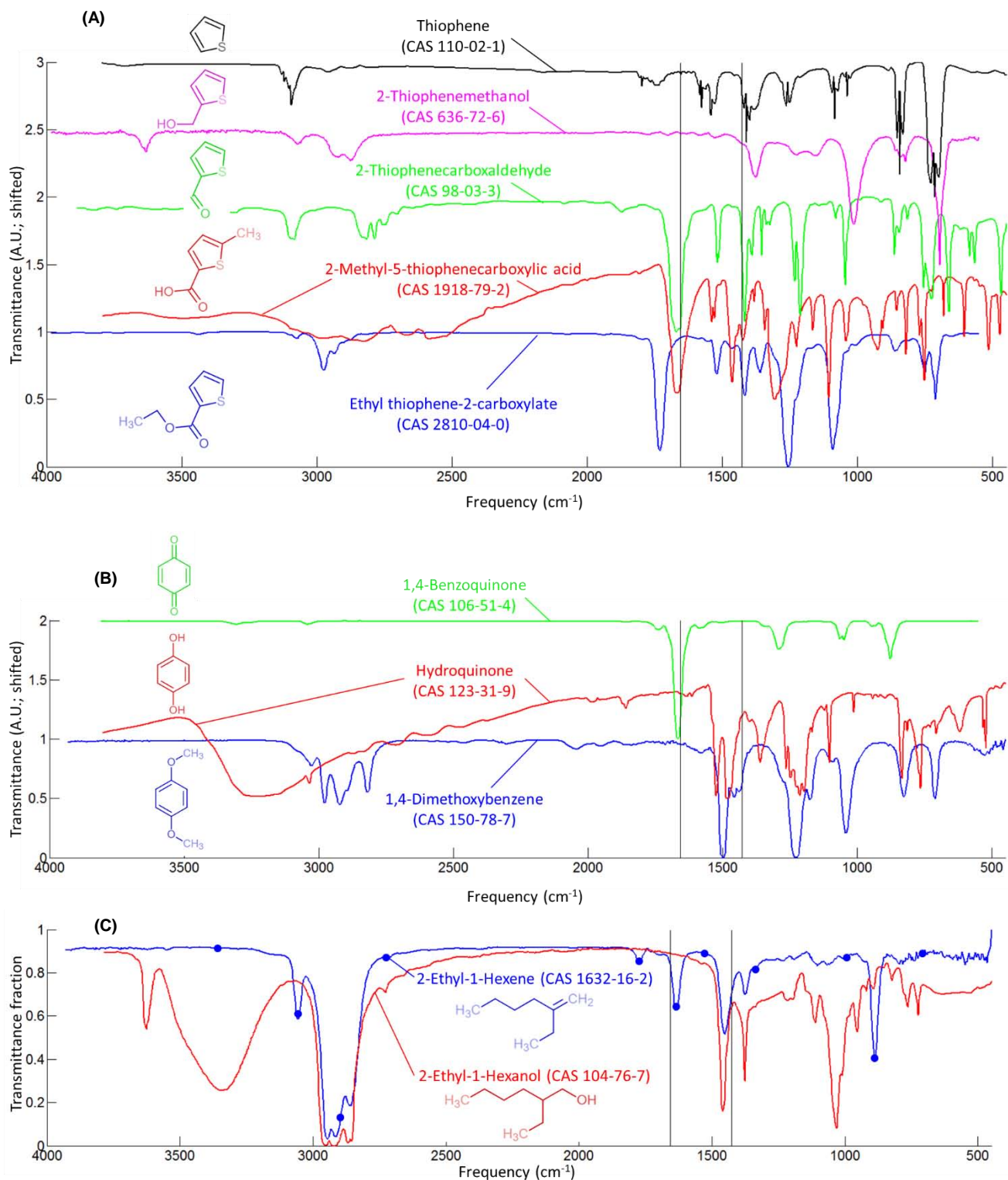


Figure S2. FT-IR spectra for possible products of a side chain cleavage reaction, reproduced from (*Linstrom & Mallard, 2017*). Vertical lines at 1656 and 1427 cm⁻¹ are included as a guide to the eye: these frequencies correspond to most significant peak growth in FT-IR of PTB7 after being annealed at high temperatures. (A) Possible products upon cleavage of the side chain on the thiophene. (B) Possible products of side chain cleavage on the benzodithiophene. (C) Possible reaction by-products (cleaved side chains). Related to Figure 2 (C).

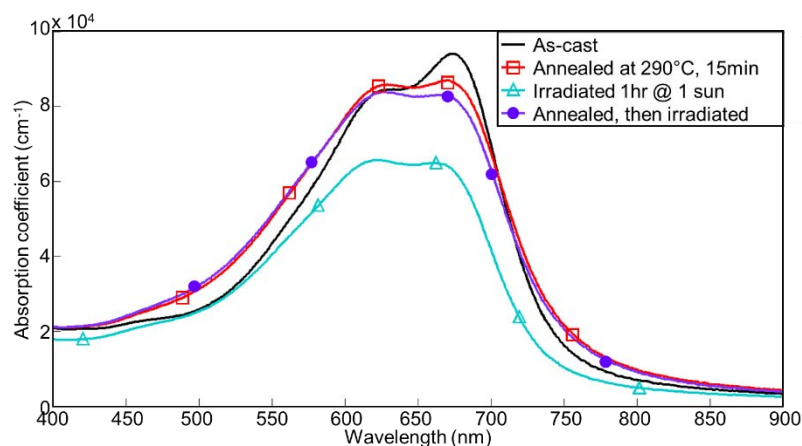


Figure S3. Comparison of UV-Vis from as-cast, annealed, and irradiated films. Data has been normalized as described above. Annealed+irradiated sample (purple) follows the same procedures as annealed (red) and irradiated (teal). Related to Figure 4 (C).

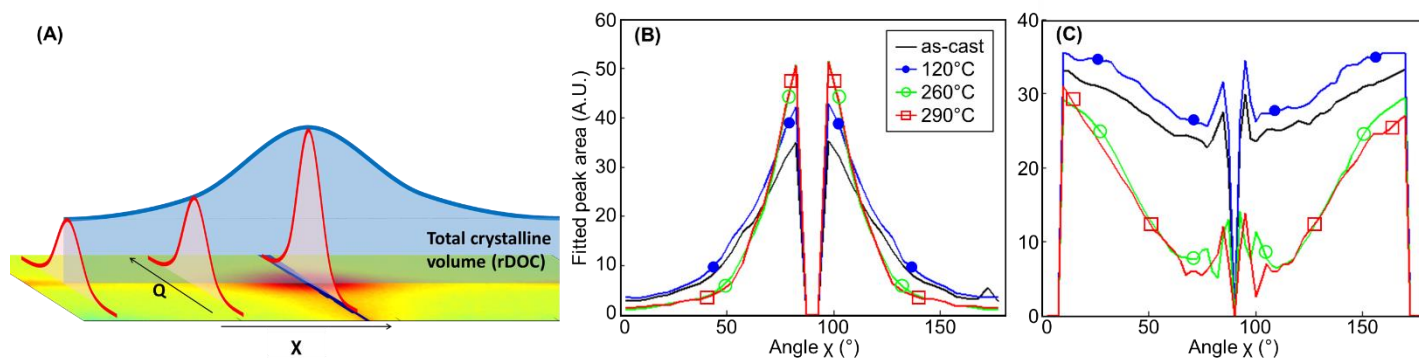


Figure S4. (A) Illustration of peak fitting approach for calculating pole figures (blue curve). The image is shown on a Q - χ coordinate system. (B) Background-corrected scattering intensity between $Q=1.35$ and 1.85 \AA^{-1} corresponding to the π - π stacking peak, with 90° as the out-of-plane direction. (C) Background-corrected scattering intensity between $Q=0.24$ and 0.6 \AA^{-1} , corresponding to the alkyl scattering peak. For the alkyl peak, increase in scattering above 70° (below 110°) is the result of direct beam reflection. Scattering below 10° (above 170°) is artificially enhanced by Yoneda peak scattering, and these angles have been omitted from (C) for clarity. Related to Figure 3.

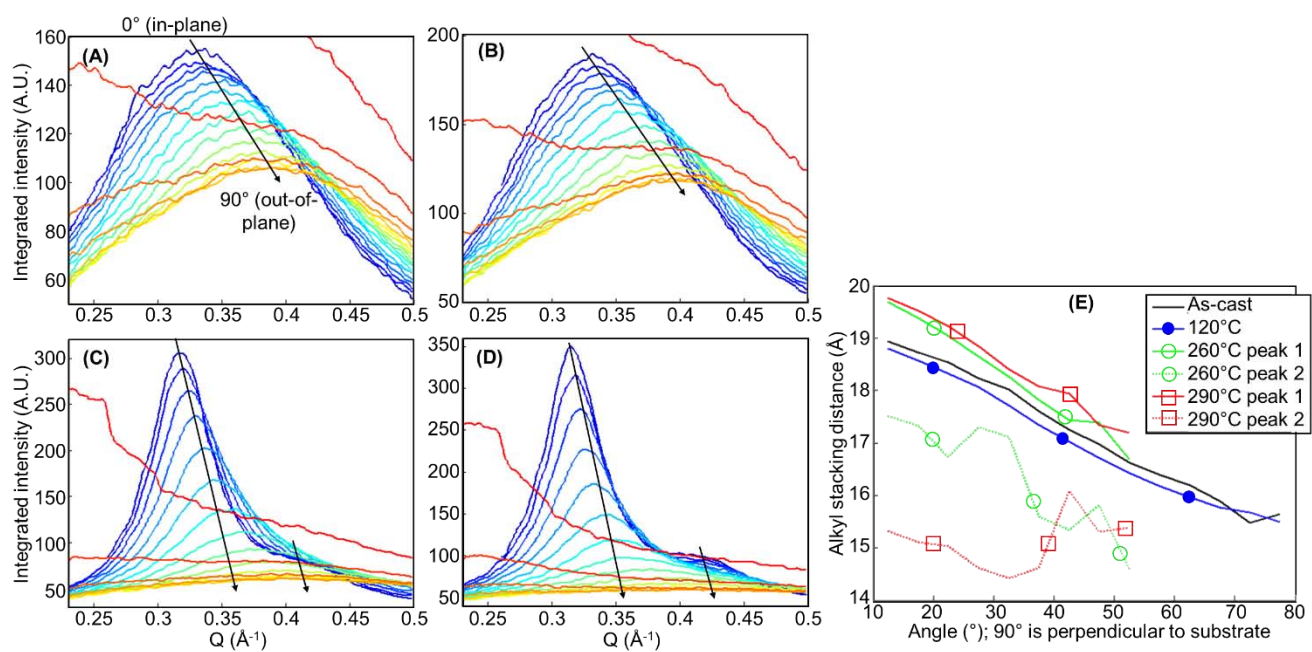


Figure S5. (A-D) I vs Q plots of the alkyl stacking peak at different polar angles for (A) as-cast, (B) 120°C annealed, (C) 260°C annealed, and (D) 290°C annealed samples. Out-of-plane data (approaching 90°—shown in red) is dominated by beam scattering effects, so fitting results are inaccurate in these regions. (E) Alkyl stacking distance versus orientation, calculated from a fit to (A-D). The single broader peak in the as-cast and 120°C annealed samples is at an intermediate position between the two resolvable peaks in the 260°C and 290°C annealed samples. For all samples, the alkyl stacking distance decreases as the angle from the substrate increases. Related to Figure 3.

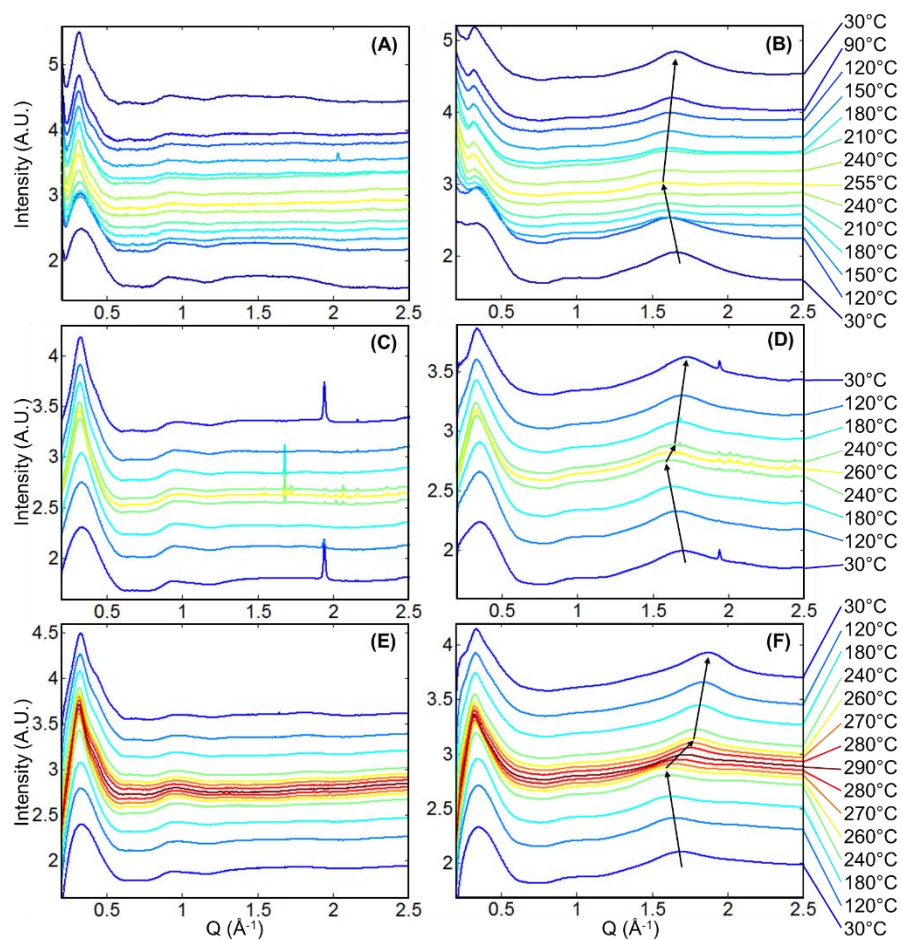


Figure S6. In-situ annealing of neat PTB7. In each figure, bottom curve represents the initial measurement (as-cast) and top curve is the final measurement after heating and cooling; black arrows show the evolution of the π - π stacking peak in time. Curves are artificially shifted by an amount proportional to the change in temperature. (A,C,E) In-plane integration from $\chi=5$ - 20° (and 160 - 175°) during heating and cooling. (B,D,F) Out-of-plane integration from $\chi=75$ - 105° during heating and cooling. (A,B) Heating to 255°C (using different material batch, experimental setup, and calibration procedure than (C-F) (see Figure 4 (D))). (C,D) heating to 260°C (see Figure 4 (E)). (E,F) Heating to 290°C (see Figure 4 (F)). Legends on the right hand side are consistent for each row. Related to Figure 4 (D-F).

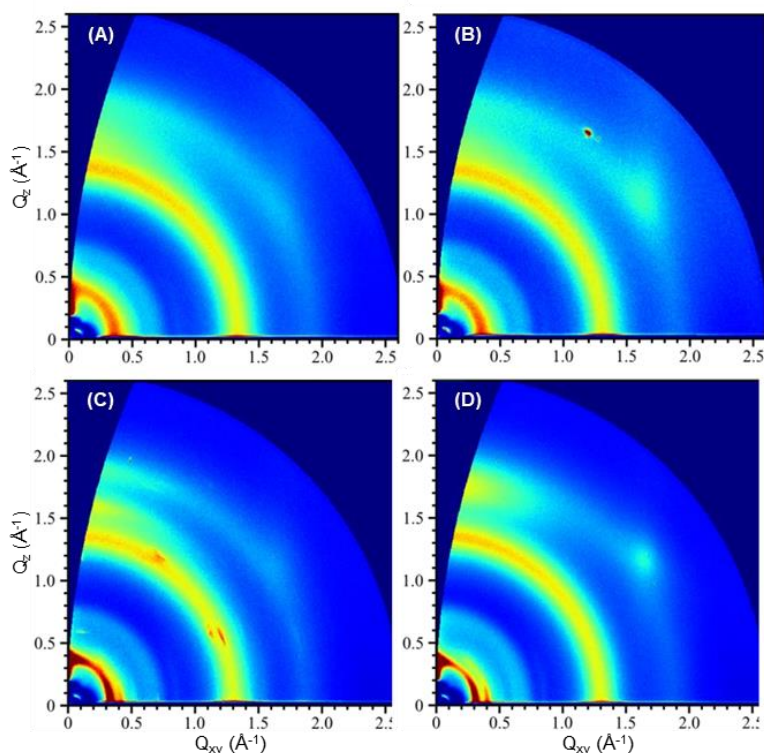


Figure S7. 2D scattering pattern for PTB7:PC₇₁BM BHJ films: (A) as-cast, (B) 120°C anneal, (C) 260°C anneal, (D) 290°C anneal. Images are plotted with intensity (detector counts) on a logarithmic scale. Each image represents a 2 or 3 minute exposure. The yellow spots at $Q_{xy} \approx 1.9$, $Q_z \approx 1.2 \text{ \AA}^{-1}$ are diffuse scattering from the Si substrate. Related to Figure 5.

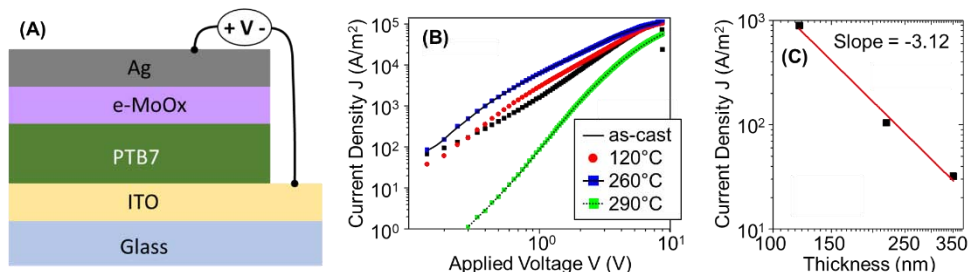


Figure S8. (A) Schematic of device used for SCLC measurements. (B) Measured J-V curves for films with different annealing temperatures, used to calculate hole mobility. Each dataset shows a clear transition to the SCLC regime where slope is close to 2 on a log-log scale. (C) Confirmation of JL^{-3} thickness dependence for the 120°C annealed sample at a bias voltage of 1.5 V (within SCLC regime). Related to Table 1.

Supplemental Tables

	Peak Position (\AA^{-1})	π - π stacking distance (\AA)
As-cast	1.69	3.72
120°C	1.68	3.74
260°C	1.68	3.74
290°C	1.80	3.49

Table S1. Positions of π - π stacking peak from fit to out-of-plane I-Q plot (before χ -correction). Related to Figure 4 (B).

Sample	Work function (eV)
ITO/PEDOT:PSS (120°C)	5.58
ITO/PEDOT:PSS (260°C)	5.43
ITO/PEDOT:PSS (290°C)	5.31

Table S2. Measurement of work function of PEDOT:PSS using Kelvin probe measurements as a function of different thermal annealing temperatures. Related to Table 1.

Transparent Methods

Materials. PTB7 was purchased from 1-Material and had a molecular weight of 92,000 Da with a polydispersity of 2.6. Chlorobenzene (HPLC grade) was purchased from Sigma Aldrich.

Preparation of thin films. The entire film fabrication procedure was performed in a nitrogen-filled glovebox. PTB7 and PC₇₁BM were dissolved in chlorobenzene by stirring on a hot plate at 60°C for at least 6 hours. The concentration used was 10 mg/mL. Blend films were prepared in a ratio of 1:1.5 PTB7:PC₇₁BM. The solutions were spin-coated directly onto clean substrates at 1000 RPM, 200 RPM/sec acceleration for 90 seconds at room temperature. Substrates were 2.5 cm² pieces cut from standard glass microscope slides for UV Vis or 1-4 cm² pieces cut from an n-doped Silicon wafer for X-Ray measurements. The thickness of films thus prepared was measured to be ~60 nm by profilometry (see Figure S1 (C)). Thermal annealing was performed by placing samples directly on a hot plate at the appropriate annealing temperature (120, 260, or 290°C) for 10-15 minutes. Samples were cooled gradually for 6-7 minutes on the hot plate after it was turned off and then quenched on a room temperature metal surface. After preparation, films used for X-Ray measurements were put in a vacuum of 10⁻⁶ mbar for at least 30 minutes, which ensured the removal of any residual solvent.

TGA. Approximately 10 mg of PTB7 powder was put in a standard TGA balance pan in TA Instrument Q500. The mass loss versus time curve for the first experiment, featuring a simple temperature ramp, is shown in Figure S1. (A).

Profilometry. The measured thickness of as-cast and annealed films is shown in Figure S1 (C). We used a Bruker Dektak 150 using 1 mg stylus force and 6.5 μm measurement range for profilometry. Nine total measurements were taken for each sample: 3 on each end and 3 in the middle. For each annealing temperature, one sample spin cast on Silicon and one sample on glass were measured (with the exception of two samples on Si for 290°C), although negligible differences were observed between the two substrates. Measurements at each position were averaged and an approximate integral was taken across the sample width to account for thickness changes across the sample. Error bars were calculated by adding the error (standard deviation of all measurements) at each position on the sample and calculating the change in the resulting integral.

FT-IR. PTB7 powder was annealed at 290°C in a metal tray covered by a glass petri dish for at least 20 minutes. Annealing was performed in a Nitrogen glovebox. As-received and annealed powders were pressed on glass microscope slides to collect FT-IR spectra on a Nicolet iS50 FT/IR Spectrometer. Attenuated total reflectance (ATR) mode was used with pellets in direct contact with the sample slot (i.e., glass slides were upside-down). The clean glass FT-IR spectrum was used as a blank.

Data was converted from absorbance to transmittance using the relation $T = 100 \cdot 10^{-A}$. The after-annealing data (blue curve) has been arbitrarily normalized for ease of comparison. More advanced normalization is not possible given the lack of control over powder properties—thickness, density, surface contact, etc.

Data from (Son, et al., 2011) has been reproduced in Figure S1 (B) (bottom two curves) along with our data to allow for direct visual comparison. This shows that the vibrational effect of side chain cleavage is similar to the effect of irradiation: both result in an increased absorption at about 1656 cm⁻¹, and a slight increase in absorption at about 1427 cm⁻¹.

To shed light on the source of these changes in FT-IR, we compared our data to FT-IR spectra tabulated in (Linstrom & Mallard, 2017). For ease of comparison, we have reproduced the data here (arbitrarily normalized). The most likely cause of the FT-IR changes is a side chain cleavage on the thiophene leaving a carboxaldehyde or carboxylic acid and/or cleaved side chain by-products trapped in the film.

UV-Vis Spectroscopy. Samples were spin-coated onto glass substrates for measurement in transmission using a Varian Cary 50 UV-VIS Spectrophotometer. To correct for thickness fluctuations, data was collected at each of three positions across each sample: one on each edge and one in the middle. The three spectra were averaged for each sample. To correct for the glass background, we used basic relationships between transmission and absorption fractions:

$$1 - A_{\text{measured}} = T_{\text{measured}} = T_{\text{film}} \cdot T_{\text{glass}} = (1 - A_{\text{film}}) \cdot (1 - A_{\text{glass}})$$

Or,

$$T_{film} = 1 - A_{film} = \frac{1 - A_{measured}}{1 - A_{glass}}$$

Where $A_{measured}$ and A_{glass} are the absorption fractions given from the raw UV-Vis spectra of the sample and the clean glass substrate respectively, A_{film} is the absorption fraction of the film alone, and T_x are the corresponding transmission fractions.

To normalize by film thickness, we applied the Beer-Lambert law, $T = e^{-\mu t}$, where T =transmission fraction, μ =absorption coefficient, and t =thickness. Combining the two equations gives:

$$\mu_{film} = \frac{-\ln\left(\frac{1 - A_{measured}}{1 - A_{glass}}\right)}{t}$$

This relationship allowed us to arrive at the wavelength-dependent absorption coefficient, with thickness measured by profilometry as previously described.

The use of direct transmission to measure UV-Vis is common in OPV literature (Schmidt-Mende & Weickert, 2016), but there is some evidence that transmission measurements may differ from the more robust integrated sphere approach for thicker films (Ehrenreich, et al., 2016). Our conclusions are based on qualitative changes to UV-Vis shape, and changes in the 290°C annealed film absorption are large enough to result in an observable color change in the film which confirms the UV-Vis measurement. Because of this, we believe that the transmission UV-Vis measurement is sufficient to support our findings in this case.

A comparison of UV-Vis from annealed and irradiated samples is shown in Figure S3. Irradiation was performed in air with a HAL-320 solar simulator from Asahi Spectra set up to generate approximately 1 sun at the sample (AM1.5G). An irradiation time of 1 hour was selected based on a visual comparison of sample color between annealed and irradiated films on glass. The sample color (and thus UV-Vis) was observed to gradually change with increased irradiation time.

Upon annealing and upon irradiation, the absorption was found to blue-shift, and the absorption intensity decreased at higher wavelengths (~676 nm) relative to lower wavelengths (~628 nm). This indicates that both processing methods have a similar effect on conjugation length in the sample. An increase in absorption width was seen with annealing; however, width was unchanged after irradiation. The irradiated film also showed an overall decrease in absorption intensity, indicating an additional photo-bleaching effect unrelated to side chain cleavage.

Annealing stabilized the sample to light-induced degradation, with additional irradiation resulting in only slight changes to the absorption. Notably, this includes a lack of photo-bleaching.

X-ray Scattering Characterization. Stanford Synchrotron Radiation Lightsource (SSRL) beamline 11-3 was used for X-Ray Diffraction. Scattering was measured in grazing incidence mode (GIWAXS) with an incident energy of 12.735 keV. For Figure 4 (D) (in-situ annealing to 255°C), the scattering was measured using a MAR345 area detector at a sample-detector distance of 400 mm, with an incident angle set to 0.12 ± 0.01 degrees from the sample surface. This incident angle is approximately equal to the critical angle of PTB7 (calculated following well-documented procedure described in (Yager, n.d.) and (Schiros, et al., 2012)), ensuring maximum diffraction (Chabinyk, 2010). All other data was measured using a MARCCD area detector at a sample-detector distance of 250 mm or 300 mm, with an incident angle set to 0.18 degrees, which minimized angle-dependent intensity error. In-situ annealing was performed using the heating stage and thermocouple attached to the sample chamber. Measurements were taken at the indicated temperatures with an uncertainty of $\pm 3^\circ\text{C}$ due to nonuniformity of heating across the sample stage. The samples were transversely shifted by a distance greater than the beam width in between 300- or 600-second scans to avoid beam damage to the sample. All measurements and annealing were performed while flowing helium through the sample chamber to avoid sample degradation and air scattering.

An LaB6 calibration scan was used to convert the 2D images to functions of the scattering vector $\mathbf{Q}=4\pi/\lambda \sin\theta$, where θ is half the scattering angle and λ is the wavelength of the incident beam. The software package WxDiff (Mannsfeld, et al., 2011) was used to reduce the data in Figure 4 (D) and Figure S7; Nika (Ilavsky, 2012) and WAXStools (Oosterhout, et al., 2017) were used for other scattering data. The vertical direction in the final image (Q_z) corresponds to out-of-plane scattering which arises from scattering planes parallel to the sample surface, and the horizontal direction (Q_{xy}) corresponds to in-plane scattering by planes perpendicular to the sample surface. The corrected images contain an inaccessible zone along Q_z due to geometry restrictions (Baker, et al., 2010).

For robust analysis, all data is normalized by exposure time, beam intensity (Monitor), film irradiation length (at small grazing incident angles, the sample length can generally be used, as the beam spreads across the entire sample), and film thickness. In general, a robust comparison of peak intensity within a scan or relative Degree of Crystallinity

between scans (rDOC) also requires multiplication by $|\cos(\chi)|$, with $\chi=90^\circ$ in the out-of-plane direction. This χ -correction assumes that the sample is isotropic in-plane and is necessary to convert scattering along the detector plane to total scattering in 3D space (Page, et al., 2014). We do not calculate rDOC in this work and hence we do not use the χ -correction. This is because the small pole figure peak width of the 260 and 290°C annealed samples makes it difficult to accurately reconstruct out-of-plane and in-plane intensity through the inaccessible zone and the horizon line respectively.

To visualize the intensity anisotropy of the π - π stacking and alkyl stacking peaks, the background along Q has to be subtracted. We used a custom algorithm which takes 5° cake slices along χ , and integrates each cake slice to give intensity versus Q. Each cake slice is fitted to a background function plus a peak function, and the area of the peak is recorded for each χ . For the π - π stacking peak, a Gaussian on a linear background was used, with an additional Gaussian peak representing Silicon substrate scattering. For the alkyl stacking peak, a Lorentzian on a falling exponential (to represent fall-off from direct beam) + flat background was used. Peak shapes were chosen based on the best fit to the data. This approach is demonstrated in Figure S4 (A).

This procedure gave the pole figures shown in Figure S4 (B,C). Annealing the samples significantly increased the anisotropy of both the alkyl and the π - π stacking peaks, indicating an increase in orientation preference.

To analyze the position anisotropy of the alkyl stacking peak, 5° cake slices were taken along χ , and each cake slice was integrated to give intensity versus Q. These curves are shown in Figure S5 (A-D). For each cake slice, the alkyl stacking peak was fitted to a Voigt curve representing the bulk of the alkyl peak plus a linear background. In data from 260 and 290°C annealed samples, the alkyl peak resolved into two peaks, so an additional Gaussian was added to the fitting. Notably, the alkyl stacking distance changes systematically with angle, from $d=19 \text{ \AA}$ ($Q=0.33 \text{ \AA}^{-1}$) in the in-plane direction to $d=16 \text{ \AA}$ ($Q=0.39 \text{ \AA}^{-1}$) at 75° from the horizon, as shown in Figure S5 (D). Literature suggests that refraction could cause a shift in out-of-plane peak positions, so we calculated the expected refractive shift using equations developed in Toney et al. (Toney & Brennan, 1989). We summed the atomic scattering factors of each atom in PTB7, tabulated in Henke et al. (Henke, et al., 1993), to approximate its complex refractive index at the X-Ray energy of 12.7 keV. The result predicted a refractive peak shift in the out-of-plane direction of 0.006 \AA^{-1} for these experimental conditions and at this Q position. This value is much smaller than the observed shift and thus the shift must be due to morphological anisotropy.

This dramatic change in alkyl spacing has been consistent in all samples measured and indicates a substrate interaction that encourages polymers to spread along the substrate and contract perpendicular to the substrate. No equivalent shift is seen in the π -stacking peak, so this effect preferentially targets the alkyl side chain interactions.

To convert the 2D images to I vs Q spectra shown in Figure 4 (A,B), the images were converted to a Q- χ coordinate system and averaged along χ . Data at $\chi=5\text{-}20^\circ$ and $160\text{-}175^\circ$ was averaged for in-plane scattering and data at $\chi=75\text{-}105^\circ$ was averaged for out-of-plane scattering.

The π - π stacking peak position was characterized by fitting the out-of-plane scattering curve between $Q=1.4$ and 1.9 \AA^{-1} to a Voigt function and linear background. The results of this fitting are shown in Table S1. The χ -correction was not used to generate these fit results, as this correction would attenuate the π - π stacking peak and make it difficult to accurately fit.

The in-situ annealing data was converted to I-Q plots by taking cake slices from $5\text{-}20^\circ$ and $160\text{-}175^\circ$ (in-plane) or $75\text{-}105^\circ$ (out-of-plane) and averaging over χ . These plots are shown in Figure S6. The π - π stacking peak was characterized by fitting the region between $Q=1 \text{ \AA}^{-1}$ and 2.5 \AA^{-1} in the out-of-plane data to a Lorentzian and linear background. This fitting was used to obtain π - π stacking distances in Figure 4 (D,E,F).

To calculate the linear Coefficient of Thermal Expansion in Figure 4 (D,E,F), the relation $CTE = \frac{1}{L_0} \frac{dL}{dT}$ was used, where L_0 is the π - π stacking distance at room temperature and dL/dT is the slope of a line fitted to the π - π stacking distance versus temperature curve.

GIWAXS data for 1:1.5 PTB7:PC₇₁BM blend films is shown in Figure S7 (A-D). Further discussion can be found in the main text.

SCLC Mobility. Space Charge Limited Current (SCLC) measurements were performed using the optimized device structure as shown in Figure S8 (A). PTB7 thin film is directly spin coated on top of plasma cleaned ITO substrates instead of using the more common PEDOT:PSS layer, since the high temperature annealing can damage PEDOT:PSS. The top electrode is optimized to be evaporated MoO_x (10 nm) and Ag (100 nm). Thermal evaporation was performed under vacuum of $\sim 10^{-6}$ mbar, through a shadow mask defining an active area of 0.08 cm^2 . PTB7 spin

coating conditions were the same as for X-Ray measurement films, and yielded an 80 nm PTB7 layer. After completing the device fabrication, the J-V characteristics were measured using a Keithley 2400 sourcemeter by applying a voltage of 0-6V, with the top MoO₃/Ag electrode as the hole injection contact. Measurement results are shown in Figure S8 (B,C).

SCLC studies require an Ohmic contact to the test material. In particular a high work function material is needed to inject holes into the deep HOMO (5.2 eV) of PTB7. A series of experiments was conducted which led to the use of glass/ITO/PTB7/MoOx/Ag as the best device structure.

The investigation of suitable contacts started with the device structure of glass/ITO/PEDOT:PSS/PTB7/MoOx/Ag. We observed a conductivity loss and a change in work function of PEDOT:PSS due to thermal annealing at temperatures considered in the present study. We attribute this to the PEDOT:PSS thermal degradation which is consistent with the literature (Vitoratos, et al., 2009). This is shown in Table S2.

Since the thermal degradation of PEDOT:PSS can lead to unreliable mobility measurements of PTB7 films spin coated on it, we considered another bottom contact constituted by evaporated MoOx (10 nm) films. Thus the second device architecture we considered was glass/ ITO/ MoOx/PTB7/ MoOx/Au. While using this architecture, we did not observe a SCLC region for all annealing temperatures, possibly because thermal annealing inside the N₂ ambient changes the oxidation state of the bottom MoOx thin films.

We therefore investigated the device architecture of glass/ITO/PTB7/MoOx/Ag, i.e a device structure in which we could benefit from the high work function of MoOx without annealing it. In this structure we observe lower current when injecting holes from the ITO side than when injecting from the MoOx side. This suggests the ITO is not making an Ohmic contact which is not surprising as its work function is lower than that of PTB7. For injection from MoOx we are able to fit to SCLC behaviour and extract the quoted mobility values. We cannot extract mobility values by injecting from the ITO because it is not making an Ohmic contact with the PTB7 films.

Time-Resolved Photoluminescence

TR-PL was performed in an inert Nitrogen environment using the frequency doubled output of a FLINT oscillator with a Yb:KGW gain medium. The laser pulses produced pulses with a fundamental frequency of 1030 nm, 100 fs FWHM, and an 80 MHz repeat rate. Perturbations to the cavity length created a Kerr lens mode-locked oscillation which produced the required signal. Photoemission frequencies were spatially separated using a Princeton Instruments SP 2300i spectrograph and detected on a Hamamatsu Streak Camera. The data was corrected for background light (no excitation) and instrumental wavelength response.

Supplemental References

Baker, J. L. et al., 2010. Quantification of Thin Film Crystallographic Orientation Using X-ray Diffraction with an Area Detector. *Langmuir*, 26(11), pp. 9146-9151.

Chabinyk, M., 2010. *Gixs-calculator Tool*, s.l.: s.n.

Ehrenreich, P. et al., 2016. H-aggregate analysis of P3HT thin films-Capability and limitation of photoluminescence and UV/Vis spectroscopy. *Scientific Reports*, Volume 6, p. 32434.

Henke, B. L., Gullikson, E. M. & Davis, J. C., 1993. X-Ray Interactions: Photoabsorption, Scattering, Transmission, and Reflection at $E = 50\text{-}30,000$ eV, $Z = 1\text{-}92$. *At. Data Nucl. Data Tables*, 54(2), pp. 181-342.

Ilavsky, J., 2012. Nika: software for two-dimensional data reduction. *J. Appl. Cryst.*, Volume 45, pp. 324-328.

Linstrom, P. J. & Mallard, W. G., 2017. *NIST Chemistry WebBook, NIST Standard Reference Database Number 69*. Gaithersberg MD, 20899: National Institute of Standards and Technology.

Mannsfeld, S. C. B., Tang, M. L. & Bao, Z., 2011. Thin Film Structure of Triisopropylsilylethynyl-Functionalized Pentacene and Tetraceno[2,3-b]thiophene from Grazing Incidence X-Ray Diffraction. *Adv. Mater.*, 23(1), pp. 127-131.

Oosterhout, S. D. et al., 2017. Mixing Behavior in Small Molecule:Fullerene Organic Photovoltaics. *Chem. Mater.*, 29(7), p. 3062–3069.

Page, K. A. et al., 2014. Confinement-Driven Increase in Ionomer Thin-Film Modulus. *Nano Lett.*, 14(5), pp. 2299-2304.

Schiros, T. et al., 2012. Reticulated Organic Photovoltaics. *Adv. Funct. Mater.*, 22(6), pp. 1167-1173.

Schmidt-Mende, L. & Weickert, J., 2016. *Organic and Hybrid Solar Cells: An Introduction*. s.l.:Walter de Gruyter GmbH & Co KG.

Son, H. J. et al., 2011. Synthesis of Fluorinated Polythienothiophene-co-benzodithiophenes and Effect of Fluorination on the Photovoltaic Properties. *J. Am. Chem. Soc.*, 133(6), pp. 1885-1894.

Toney, M. F. & Brennan, S., 1989. Observation of the effect of refraction on x rays diffracted in a grazing-incidence asymmetric Bragg geometry. *Phys. Rev. B*, 39(11), pp. 7963-7966.

Vitoratos, E. et al., 2009. Thermal degradation mechanisms of PEDOT:PSS. *Organic Electronics*, 10(1), pp. 61-66.

Yager, K., n.d. *Critical Angle*. [Online] Available at: http://gisaxs.com/index.php/Critical_angle [Accessed 6 June 2017].